JOURNAL OF AIRCRAFT
Vol. 34, No. 4, July–August 1997

Influence of Shaft Angle of Attack on Sound Radiation by Subsonic Propellers

Jeffrey J. Kelly* and L. Cathy Nguyen†
Lockheed Martin Engineering and Sciences, Hampton, Virginia 23681-0001

The formulation to account for effects of propeller angle of attack on acoustic radiation by propellers is presented. A propeller operating at an angle of attack presents a nonuniform inflow situation that is known to have a pronounced influence on noise. Noise predictions, based on this new formulation, are compared with measured wind-tunnel data. Predictions for observers fixed in the propeller plane are also included to assess the influence of shaft angle of attack.

Nomenclature

c_0 = ambient speed of sound
f = function defining blade surface
$\boldsymbol{l}$ = local force per unit area of blade acting on fluid
l_r = component of loading vector in direction of radiation vector, $l_i r_i$
M = source Mach number
M_r = component of source Mach vector in direction of radiation vector, $M_i \hat{\boldsymbol{r}}_i$
$\boldsymbol{n}$ = blade surface normal vector
p = acoustic pressure
p_L = acoustic pressure produced by loading
p_T = acoustic pressure produced by thickness
$\boldsymbol{r}$ = distance from source point at emission time to observer
$\hat{\boldsymbol{r}}$ = unit vector in direction $\boldsymbol{r}$
S = surface area
t = time the noise signal is received by observer
$\boldsymbol{V}_F$ = forward velocity of aircraft
$\boldsymbol{v}$ = source velocity vector
v_n = source velocity component in direction of blade normal, $v_i n_i$
$\boldsymbol{x}$ = observer position in ground fixed frame
$\boldsymbol{y}$ = source position in ground fixed frame
α = angle of attack of propeller shaft
$\boldsymbol{\eta}$ = source position in blade fixed frame
τ = time at which noise signal is emitted at source position
ψ = angle between x_1 and η_1 axes, $\Omega\tau$
Ω = angular velocity of blade

Introduction

CONTINUING growth in general aviation and commuter aircraft operations has prompted a renewed interest in the noise associated with these aircraft. Reference 1 provides a recent assessment of the noise reduction technology progress and needs for this class of airplanes. Nonuniform inflow as a result of propeller operating conditions and installation on the airplane can significantly affect the sound field. Shaft angle of attack is an example of operating conditions that produce inflow distortion. Nonuniform inflow to a propeller produces unsteady blade loading that can result in a pronounced increase in noise. This effect has been noted in theoretical analysis[2] as well as in laboratory experiments.[3,4]

References 5–7 document results of previous studies related to the prediction of the influence of propeller angle of attack on radiated noise. The procedure used in Ref. 5 corrects the blade loading to account for the nonuniform inflow resulting from propeller angle of attack, but ignores the angle of attack in the acoustic model. References 6 and 7 contain noise predictions for propellers at an angle of attack. The present study implements these procedures in the NASA Aircraft Noise Prediction Program (ANOPP)–Propeller Analysis System (PAS).[8,9] The predicted results are compared with measurements from wind-tunnel tests.

The ANOPP–PAS computer code comprises computational modules that can calculate the aerodynamics, performance, and noise of propellers. Previous studies describe the prediction capabilities, features, and improvements to the original system.[10,11] The elements of ANOPP–PAS that were relevant to this study are the modules that predict the propeller loads and the noise module. Descriptions of the modules and their attendant theories can be found in Ref. 8. To compute the blade loading and, therefore, the noise, the induced velocity field of the propeller is required. Calculation of the induced flow is accomplished with the propeller axis at zero angle of attack. After which, the kinematic effect of shaft angle of attack is included by a rotational transformation of the total velocity field. The main concern of the analysis presented in this paper is the modification of the noise model to include shaft angle of attack.

Noise Model

The noise module in ANOPP–PAS is based on formulation 1A of Farassat[12,13]

$$4\pi p_L(\boldsymbol{x}, t) = \frac{1}{c_0}\int_{f=0}\left[\frac{l_i\hat{\boldsymbol{r}}_i}{r(1-M_r)^2}\right]_\tau \mathrm{d}S + \int_{f=0}\left[\frac{l_r - l_i M_i}{r^2(1-M_r)^2}\right]_\tau \mathrm{d}S + \frac{1}{c_0}\int_{f=0}\left[\frac{l_r(r\dot{M}_i\hat{\boldsymbol{r}}_i + c_0 M_r - c_0 M^2)}{r^2(1-M_r)^3}\right]_\tau \mathrm{d}S \tag{1a}$$

$$4\pi p_T(\boldsymbol{x}, t) = \int_{f=0}\left[\frac{\rho_0 v_n(r\dot{M}_i\hat{\boldsymbol{r}}_i + c_0 M_r - c_0 M^2)}{r^2(1-M_r)^3}\right]_\tau \mathrm{d}S \tag{1b}$$

where

$$p(\boldsymbol{x}, t) = p_L(\boldsymbol{x}, t) + p_T(\boldsymbol{x}, t) \tag{1c}$$

Received Sept. 29, 1996; presented as Paper 97-0381 at the AIAA 35th Aerospace Sciences Meeting, Reno, NV, Jan. 6–9, 1997; revision received March 22, 1997; accepted for publication March 24, 1997.

*Staff Engineer, NASA Langley Research Center, M/S 303. Senior Member AIAA.
†Senior Engineer, M/S 303, NASA Langley Research Center.

For propellers, this formulation predicts discrete tones at harmonics of the blade passage frequency (BPF). Here, p_L and p_T represent acoustic pressures caused by blade loading and thickness, respectively. The terms in brackets are evaluated on the surface $f = 0$ (blade surface) at the emission time τ and integrated over the blade surface elements dS. Therefore, for each instant of reception time t, at a particular observer location $\boldsymbol{x}$, it must be determined where every element of the surface was when it emitted the received signal. Since the geometry and the kinematics of the blade are known and it is assumed that the signals travel at the ambient speed of sound, it is feasible to compute τ for each surface element, and thus, evaluate the previous integrals. Connecting all of the blade elements at their emission (retarded) times generates a surface distorted from the physical planform to a shape called the acoustic planform.[14]

Since the integrands depend on vector operations, appropriate reference frames must be established. Three reference frames, which are illustrated in Fig. 1, are employed in the computational scheme. These frames are the ground (medium) fixed $\boldsymbol{x}$ frame, the aircraft fixed $\boldsymbol{X}$ frame, and the blade fixed $\boldsymbol{\eta}$ frame. At the initial time, the propeller hub is located at the origin of the $\boldsymbol{x}$ frame. The x_3 axis defines the flight direction. Initially, the $\boldsymbol{X}$ frame coincides with the $\boldsymbol{x}$ frame, but afterward translates at the constant rate $\boldsymbol{V}_F$, the aircraft forward velocity. Operations involving blade normals or surface pressures are more easily computed in the $\boldsymbol{\eta}$ frame. It is more convenient to express the source position $\boldsymbol{y}$ in the $\boldsymbol{x}$ frame, then compute $\boldsymbol{r} = \boldsymbol{x} - \boldsymbol{y}$ and $\hat{\boldsymbol{r}} = \boldsymbol{r}/r$ in the $\boldsymbol{x}$ frame and transform the vector components to the $\boldsymbol{\eta}$ frame. Thus, in addition to the orthogonal transformation based on the propeller rotational angle ψ, an orthogonal transformation defined by α must be accounted for to relate quantities in the $\boldsymbol{\eta}$ frame to those in the $\boldsymbol{x}$ frame.

Considering Eq. (1), it is seen that the quantities that need to be revised to include angle of attack are $\boldsymbol{r}$, $\hat{\boldsymbol{r}}$, v_n, and $\boldsymbol{M}$. Note that v_n and $\boldsymbol{M}$ are based on source absolute velocity. No correction is needed for the source absolute acceleration $\boldsymbol{M}$, since the aircraft forward velocity $\boldsymbol{V}_F$ is constant. Also, the retarded time equation, which must be solved to establish emission time τ for each observer time t, has to be formulated to include angle of attack. From Fig. 1, it is seen that the observer and source locations in the x frame are, respectively,

$$\boldsymbol{x} = \boldsymbol{V}_F t + \boldsymbol{x}_0 \tag{2}$$

$$\boldsymbol{y} = \boldsymbol{V}_F \tau + T_\alpha T_\psi \boldsymbol{\eta} \tag{3}$$

Here, the coordinate transformation matrices are given by

$$T_\psi = \begin{bmatrix} \cos\psi & -\sin\psi & 0 \\ \sin\psi & \cos\psi & 0 \\ 0 & 0 & 1 \end{bmatrix} \tag{4}$$

$$T_\alpha = \begin{bmatrix} \cos\alpha & 0 & \sin\alpha \\ 0 & 1 & 0 \\ -\sin\alpha & 0 & \cos\alpha \end{bmatrix} \tag{5}$$

Notice that the source position vector is now dependent on α.

The matrix form of Eq. (3) is

$$\begin{bmatrix} y_1 \\ y_2 \\ y_3 \end{bmatrix} = \begin{bmatrix} \cos\alpha\cos\psi & -\cos\alpha\sin\psi & \sin\alpha \\ \sin\psi & \cos\psi & 0 \\ -\sin\alpha\cos\psi & \sin\alpha\sin\psi & \cos\alpha \end{bmatrix} \times \begin{bmatrix} \eta_1 \\ \eta_2 \\ \eta_3 \end{bmatrix} + \begin{bmatrix} 0 \\ 0 \\ V_F\tau \end{bmatrix} \tag{6}$$

The previous relations allow the radiation vector, given by

$$\boldsymbol{r} = \boldsymbol{x} - \boldsymbol{y} \tag{7}$$

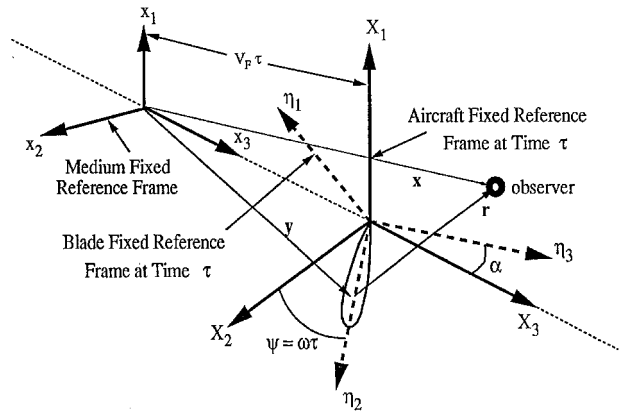

Fig. 1 Reference frames.

to be computed in the $\boldsymbol{x}$ frame. But $\boldsymbol{r}$ must be transformed to the $\boldsymbol{\eta}$ frame for the calculation of p according to Eq. (1). This transformation is

$$\begin{bmatrix} r_1 \\ r_2 \\ r_3 \end{bmatrix}_\eta = T_\psi^{-1} T_\alpha^{-1} \begin{bmatrix} r_1 \\ r_2 \\ r_3 \end{bmatrix}_x \tag{8}$$

where

$$T_\psi^{-1} T_\alpha^{-1} = T_\psi^T T_\alpha^T = \begin{bmatrix} \cos\psi\cos\alpha & \sin\psi & -\cos\psi\sin\alpha \\ -\sin\psi\cos\alpha & \cos\psi & \sin\psi\sin\alpha \\ \sin\alpha & 0 & \cos\alpha \end{bmatrix} \tag{9}$$

since T_ψ and T_α are orthogonal matrices.

The absolute velocity for each source point is expressed as

$$\boldsymbol{v} = \boldsymbol{V}_F + \boldsymbol{\Omega} x \boldsymbol{\eta} \tag{10}$$

In the $\boldsymbol{\eta}$ frame, Eq. (10) can be written as

$$\boldsymbol{v} = T_\psi^T T_\alpha^T \begin{bmatrix} 0 \\ 0 \\ V_F \end{bmatrix} + \boldsymbol{\Omega} x \boldsymbol{\eta} \tag{11}$$

From Eq. (11), it is found that the components of $\boldsymbol{v}$ are

$$\begin{bmatrix} v_1 \\ v_2 \\ v_3 \end{bmatrix} = \begin{bmatrix} -\Omega\eta_2 - V_F\sin\alpha\cos\psi \\ \Omega\eta_1 + V_F\sin\alpha\sin\psi \\ V_F\cos\alpha \end{bmatrix} \tag{12}$$

As indicated in Eq. (1), emission times must be found for the retarded time equation:

$$|\boldsymbol{x}(t) - \boldsymbol{y}(\tau)|^2 = c_0^2 (t - \tau)^2 \tag{13}$$

Using Eqs. (2) and (3) allows the previous relation to be stated in terms of $\boldsymbol{\eta}$-frame components as

$$|T_\psi^T T_\alpha^T [\boldsymbol{x}_0 + \boldsymbol{V}_F(t - \tau)] - \boldsymbol{\eta}|^2 = c_0^2 (t - \tau)^2 \tag{14}$$

where

$$T_\psi^T T_\alpha^T [\boldsymbol{x}_0 + \boldsymbol{V}_F(t - \tau)] = T_\psi^T T_\alpha^T \begin{bmatrix} x_1 \\ x_2 \\ x_3 + V_F(t - \tau) \end{bmatrix} \tag{15}$$

Table 1 Test matrix

Run no.	Pitch three-quarter radius, deg	Ω, rpm	V_F, mps	Power, kW	Thrust, N	α, deg	Helical Mach no.
1	19.9	2100	51.2	95.9	1520	0	0.6729
2	19.9	2100	51.6	97.9	1481	−3.6	0.6746
3	19.9	2100	51.4	97.9	1540	−7.3	0.6764
4	19.9	2100	51.6	94.8	1461	3.8	0.6734
5	19.9	2100	51.4	97.0	1515	7.4	0.6751

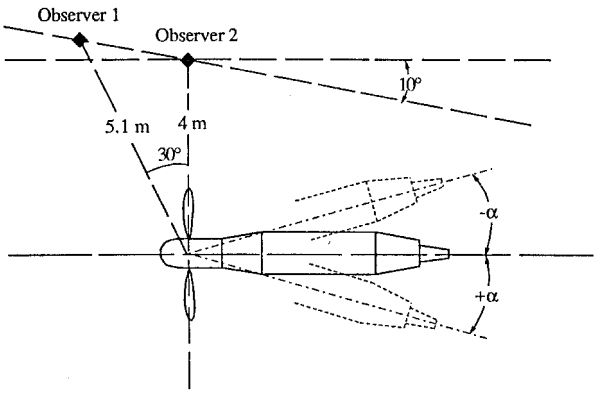

Fig. 2 Microphone positions relative to propeller in the DNW test.

Using the substitutions given by

$$\phi = \Omega(\tau - t), \qquad x_1^* = x_1 \cos\alpha - x_3 \sin\alpha$$

$$x_3^* = x_3 \cos\alpha - x_1 \sin\alpha, \qquad x^* = \sqrt{x_1^{*2} + x_2^2}$$

$$\eta = \sqrt{\eta_1^2 + \eta_2^2}, \qquad \psi_x = \tan^{-1}(x_2/x_1^*), \qquad \psi_\eta = \tan^{-1}(\eta_2/\eta_1)$$

results in the following retarded time relation by way of Eq. (14):

$$A\phi^2 + B\phi + C + \cos(\phi + D) + E\phi\cos(\phi + F) = 0 \qquad (16)$$

where

$$A = \frac{c_0^2 - V_F^2}{2\eta x^* \Omega^2}, \qquad B = \frac{V_F[-x_1^* \sin\alpha + (x_3^* - \eta_3)\cos\alpha]}{\Omega\eta x^*}$$

$$C = -\frac{[x^{*2} + \eta^2 + (x_3^* - \eta_3)^2]}{2x^*\eta}, \qquad D = \psi_\eta - \psi_x + \Omega t$$

$$E = \frac{V_F \sin\alpha}{\Omega x^*}, \qquad F = \psi_\eta + \Omega t$$

Because this study concerns only subsonic propellers, there exists a single solution for $\phi < 0$ (causality) to Eq. (16). This particular root of Eq. (16) was found by Newton's method. With the previous relations, Eq. (1) is readily integrated numerically and the influence of shaft angle of attack can be assessed.

Comparisons of Predictions with Test Data

Prediction results from PAS are now compared to propeller noise tests that were performed in the Deutsch-Niederlaendischer Windkanal (DNW) wind tunnel. For a description of the test and displays of the measured acoustic data see Ref. 15. This test involved two propellers manufactured by Hartzell that were two-bladed and had diameters of 2.03 m. Clark Y airfoil sections describe the blade geometry of both propellers. The F8475 D-4, which is the production version used on the Piper Cherokee Lance Aircraft, has a thin round tip with a thickness ratio of 6.4% at the three-quarter radius location. The

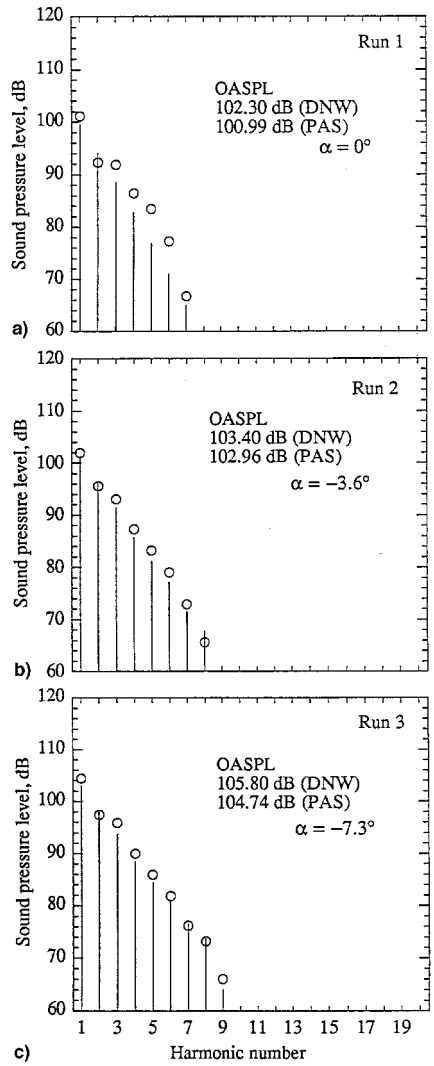

Fig. 3 Comparison of prediction with data at observer 1: |, PAS; ○, DNW.

F9684-14 has a square tip with a thickness ratio of 8.5% at the three-quarter radius location.

Table 1 contains test conditions for selected runs for the round-tip propeller. The primary variable in these runs is the propeller angle of attack. The blade geometry, pitch angle, rpm, propeller angle of attack, and aircraft speed were used as input to PAS to predict the spectra for the test runs in Table 1. Figure 2 illustrates the test setup that is simulated in the PAS predictions. Microphones were located at the observer 1 and 2 positions. As shown in Fig. 2, +α designates a nose-down propeller configuration to the observers and −α a nose-up orientation to the observers. Observer 2 is situated in the propeller plane for α = 0 deg.

Figure 3 depicts spectra measured at observer 1 for α = 0 deg and two nose-up angles, α = −3.6 and −7.3 deg. Spectral lines occur at harmonics of the BPF, 70 Hz. Here, the observer

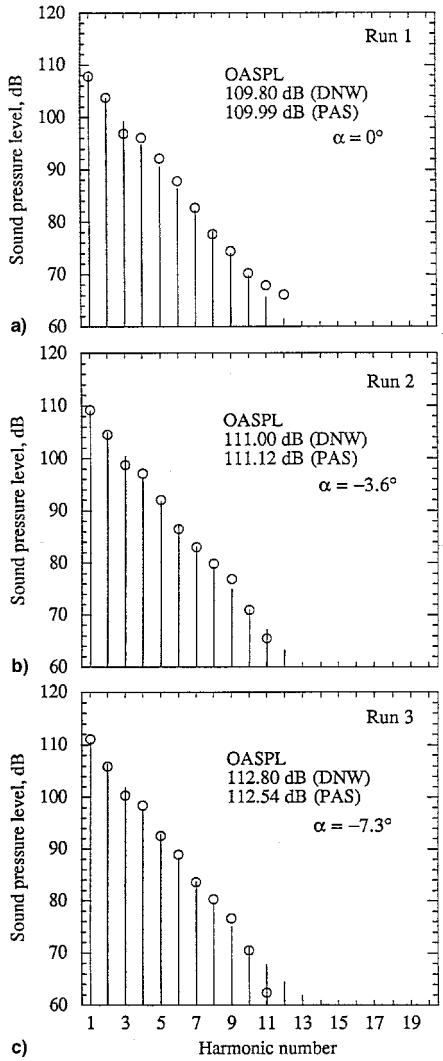

Fig. 4 Comparison of prediction with data at observer 2: |, PAS; ○, DNW.

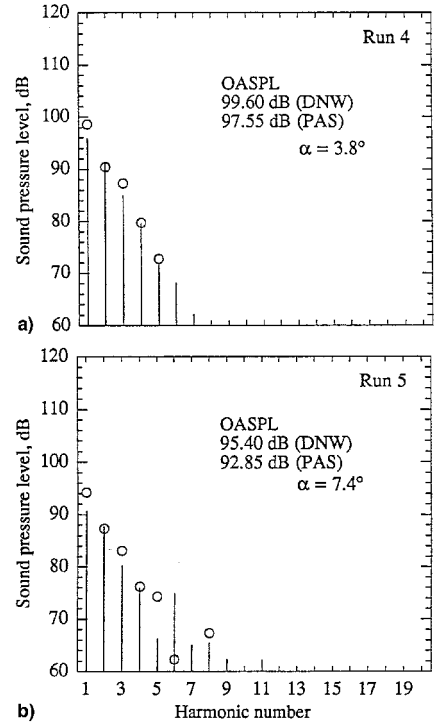

Fig. 5 Comparison of prediction with data at observer 1: |, PAS; ○, DNW.

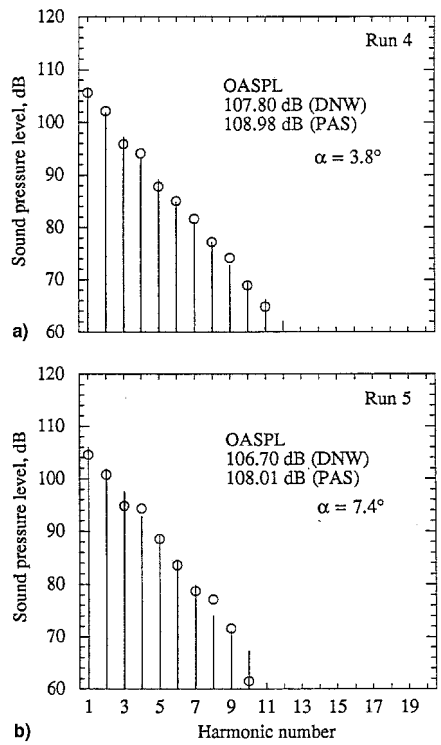

Fig. 6 Comparison of prediction with data at observer 2: |, PAS; ○, DNW.

is always upstream of the propeller plane. The noise levels increase with α. The peak sound–pressure levels (SPL), which occur at the BPF, increase by approximately 3 dB for both the experimental and predicted data for $\alpha = -7.3$ deg, compared to $\alpha = 0$ deg. The systematic increase in overall sound–pressure level (OASPL) are displayed on each spectrum. The number of harmonics used to compute OASPL are the same for both data in each run. This number is dictated by the noise floor of the DNW measurements.

Figure 4 shows predicted and measured noise at observer 2 for the same runs (operating conditions) that were displayed in Fig. 3. For these cases, the observer is downstream of the propeller plane for nonzero values of α. The SPLs are appreciably higher at observer 2 and the levels increase with propeller angle of attack. The PAS predictions at the three propeller angles of attack are in good agreement with the test data.

Figures 5 and 6 show the noise spectra at observers 1 and 2, respectively, for positive angle-of-attack configurations of the propeller shaft so that both observers are upstream of the propeller disk. At observer 1, the measured OASPL decreases by 6.8 dB when the propeller angle of attack changes to +7.4 deg from 0 deg (Fig. 3a). The PAS-predicted levels decrease by 8 dB for the same change in angle of attack. At observer 2, the measured OASPL decreases by 3.1 dB, whereas the predicted OASPL decreases by 2 dB because of the change in propeller angle of attack (Fig. 6). Again, the noise levels decrease with increasing angle of attack, but only slightly.

Angle of Attack Effects Relative to Propeller Disk

Next, predictions from PAS are presented for observers fixed relative to the propeller plane to demonstrate the effects of shaft angle of attack. This also eliminates any differences resulting from spherical spreading. Figure 7 depicts a geometrical description of the simulation. All three observers are the same distance (4 m) from the propeller hub. Observer 1 is situated 30 deg in front of the propeller disk, observer 2 is in

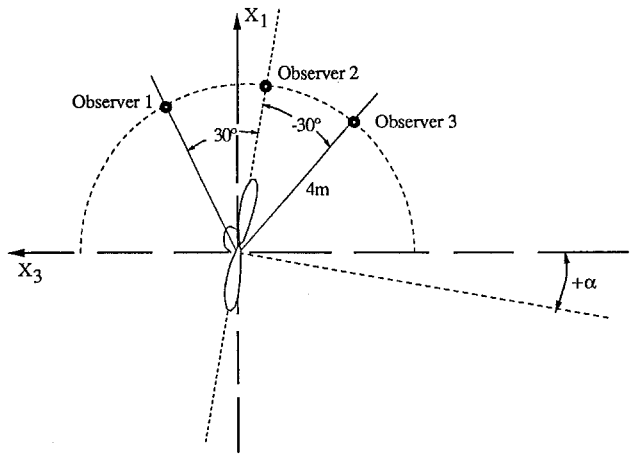

Fig. 7 Simulation geometry for observers fixed relative to propeller plane.

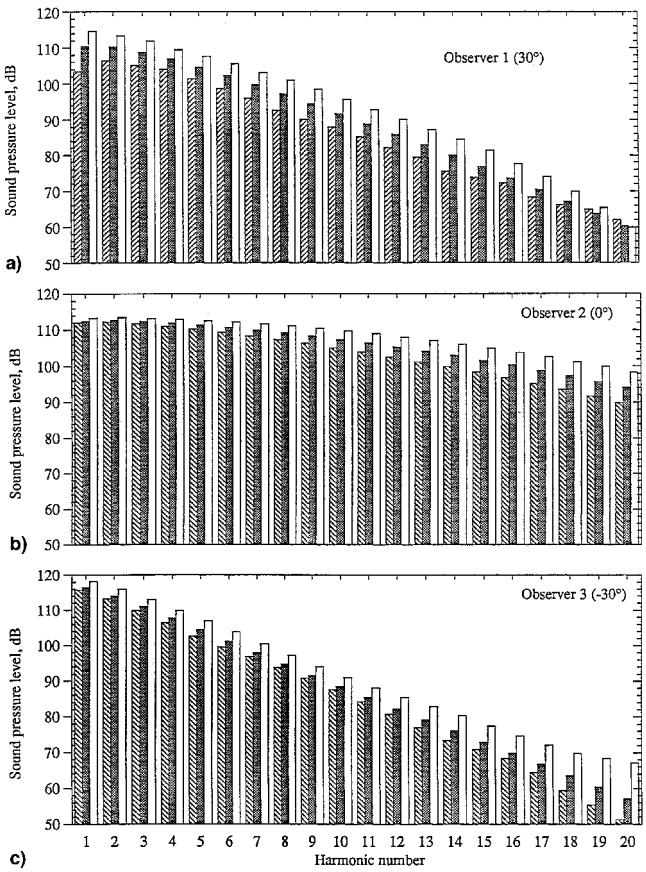

Fig. 8 Predicted spectra for observers fixed relative to the disk plane, three-quarter root pitch angle = 19.90 deg, V_F = 77.3 m/s, Ω = 2700 rpm, ▨ α = 5 deg, ■ α = 0 deg, □ α = −5 deg.

the propeller plane, and observer 3 is 30 deg aft of the disk plane. PAS-predicted noise spectra for α = −5, 0, and 5 deg are illustrated in Fig. 8. Here, the spectral lines appear at harmonics of 90 Hz (BPF). This figure and Table 2 show that the peak SPL (first harmonic) for each α is attained at observer 3 (−30 deg). But OASPL is maximum in the propeller plane (observer 2) because of the greater levels of the higher harmonics. For each direction, the highest levels are associated with the nose-up configuration (α = −5 deg), which, in general, was also observed in the prediction and data comparisons in the previous section. Figure 8a shows α strongly influencing BPF levels upstream of the propeller disk. The levels span 12

Table 2 Predicted sound–pressure levels relative to propeller disk

Observer	α, deg	Peak SPL, dB	Peak harmonic	OASPL, dB	OASPL, dBA
1	−5	114.7	1	119.5	105.8
1	0	110.4	1	116.1	102.5
1	5	106.4	2	111.9	99.0
2	−5	113.4	2	123.0	116.2
2	0	112.6	2	121.4	113.8
2	5	112.3	2	120.3	111.7
3	−5	118.2	1	121.6	104.9
3	0	116.5	1	119.7	102.6
3	5	115.8	1	118.9	101.4

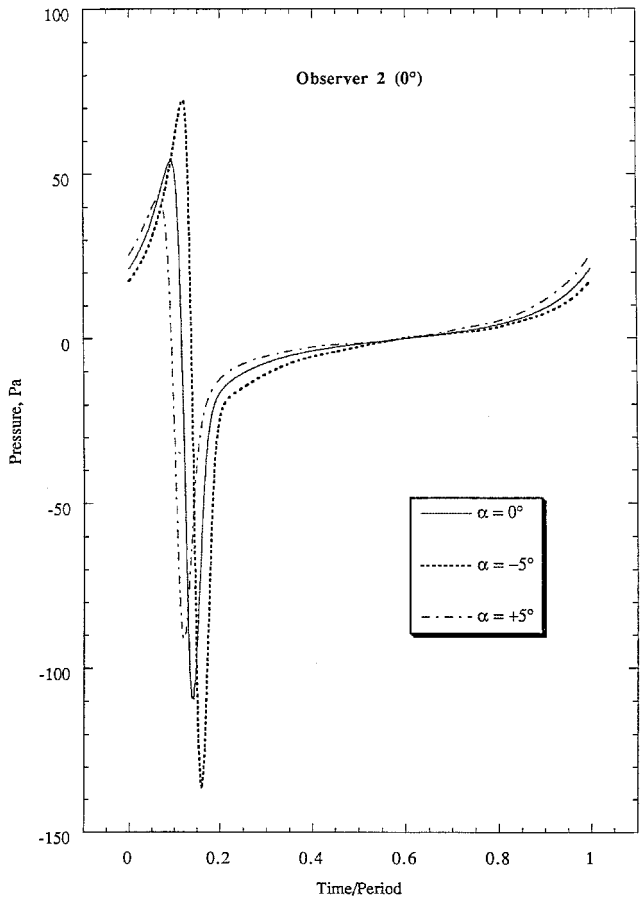

Fig. 9 Pressure–time history.

dB and this wide range is probably caused by unsteady loading noise.

It is apparent from Fig. 8 that the change in α causes greater changes in higher harmonic SPLs and smaller changes in lower harmonic SPLs for observers 2 and 3. This hints that *A* weighting could be strongly affected by α. Table 2 contains *A*-weighted OASPL for the cases under discussion. The angle-of-attack effects are of the order 4.5 dBA for observer 2 and 3.5 dBA for observer 3. Figure 9 shows the pressure–time histories corresponding to the spectra of Fig. 8b, observer 2. Propeller angle of attack α affects the amplitude and phase of the time series, but the signals are quite similar. This was also true of the other two observer locations. From Fig. 9 it can be deduced that the impulsive nature of the acoustic pressure accounts for the significant higher harmonic content exhibited in Fig. 8b.

Summary

The formulation of shaft angle of attack into sound radiation models of propellers was presented. This model was imple-

mented in the ANOPP–PAS computer code. Comparisons of PAS predictions with measured wind-tunnel data showed that, in general, noise levels increased with increasing nose-up configuration and decreased with increasing nose-down configuration. Noise levels were higher for noise-up orientations. Also included in this paper are predictions for observers fixed relative to the propeller disk that reflect shaft angle-of-attack effects. Spectra and pressure–time histories were constructed for upstream, downstream, and in-plane observers. Peak SPL occurred at the downstream observer for the angles of attack considered, but highest OASPL was attained for the in-plane observer. Also, it was shown that, in general, shaft angle of attack had a greater influence on the higher harmonic SPLs and, consequently, on the *A*-weighted OASPL.

Acknowledgment

This study was supported by NASA Langley Research Center Contract NAS1-19000.

References

[1]Metzger, F. B., "An Assessment of Propeller Aircraft Noise Reduction Technology," NASA CR 198237, Aug. 1995.

[2]Wright, S. E., "Discrete Radiation from Rotating Periodic Sources," *Journal of Sound and Vibration*, Vol. 17, No. 4, 1971, pp. 437–498.

[3]Tanna, H. K., Burrin, R. H., and Plumblee, H. E., Jr., "Installation Effects on Propeller Noise," *Journal of Aircraft*, Vol. 18, No. 4, 1981, pp. 303–309.

[4]Block, P. J. W., and Martin, R. M., "Results from Performance and Noise Tests of Model Scale Propellers," Society of Automotive Engineers, Paper Series 830730, April 1983.

[5]Padula, S. L., and Block, P. J. W., "Predicted Changes in Advanced Turboprop Noise with Shaft Angle of Attack," *Journal of Propulsion and Power*, Vol. 1, No. 5, 1985, pp. 381–387.

[6]Dunn, M. H., and Tarkenton, G. M., "Computational Methods in the Prediction of Advanced Subsonic and Supersonic Propeller Induced Noise — ASSPIN Users' Manual," NASA CR 4434, April 1992.

[7]Farassat, F., Dunn, M. H., and Spence, P. L., "A Note on Advanced Propeller Noise Prediction in the Time Domain," *AIAA Journal*, Vol. 30, No. 9, 1992, pp. 2337–2340.

[8]Zorumski, W. E., and Weir, D. S. (eds.), "Aircraft Noise Prediction Program Theoretical Manual, Part 3, Propeller Aerodynamics and Noise," NASA TM 83199, June 1986.

[9]Weir, D. S., and Powers, J. O., "Comparisons of Predicted Propeller Noise with Windtunnel and Flyover Data," AIAA Paper 87-0527, Jan. 1987.

[10]Golub, R. A., and Nguyen, L. C., "A Review and Update of the NASA Aircraft Noise Prediction Program Propeller Analysis System," Society of Automotive Engineers, TP Series 891032, April 1989.

[11]Nguyen, L. C., "The NASA Aircraft Noise Prediction Program Improved Propeller Analysis System," NASA CR 4394, Sept. 1991.

[12]Farassat, F., and Succi, G. P., "The Prediction of Helicopter Rotor Discrete Frequency Noise," *Vertica*, Vol. 7, No. 4, 1983, pp. 309–320.

[13]Brentner, K. S., "Prediction of Helicopter Rotor Discrete Frequency Noise — A Computer Program Incorporating Realistic Blade Motions and Advanced Acoustic Formulation," NASA TM-87721, 1986.

[14]Hanson, D. B., "Near Field Noise of High Tip Speed Propellers in Forward Flight," AIAA Paper 76-565, July 1976.

[15]Dobrzynski, W. M., Heller, H. H., Powers, J. O., and Densmore, J. E., "DFVLR/FAA Propeller Noise Tests in the German — Dutch Wind Tunnel DNW," Federal Aviation Administration Executive Data Rept., FAA-AEE 86-3, 1986.